

Multiwavelength study of low-luminosity 6.7-GHz methanol masers *

Yuan-Wei Wu, Ye Xu and Ji Yang

Purple Mountain Observatory, Chinese Academy of Sciences, Nanjing 210008, China;
ywwu@pmo.ac.cn

Received 2010 April 11; accepted 2010 July 16

Abstract We present results of $^{13}\text{CO}(1-0)$, $\text{C}^{18}\text{O}(1-0)$, and $\text{HCO}^+(1-0)$ map observations and $\text{N}_2\text{H}^+(1-0)$ single point observations directed towards a sample of nine low-luminosity 6.7-GHz masers. N_2H^+ line emission has been detected from six out of nine sources, C^{18}O line emission has been detected from eight out of nine sources, and HCO^+ and ^{13}CO emission has been detected in all sources. In particular, a “blue profile” of the HCO^+ spectrum, a signature of inflow, is found towards one source. From integrated intensity emission maps, we identified 17 cores in the sample. Among them, nine cores are closely associated with low-luminosity methanol masers. For these cores, we derive the column densities, core sizes, masses and molecular abundances. Comparison of our results with similar molecular line surveys towards the southern sky methanol masers indicates that linewidths of our sample, including only the low-luminosity masers, are smaller than the sample that includes both low- and high-luminosity masers. For the maser associated cores, their gas masses have the same order of magnitude as their virial masses, indicating that these cores are gravitationally bound systems. In addition, we have found from our observations that the low-luminosity methanol masers tend to coexist with H_2O masers and outflows rather than with OH masers.

Key words: masers — ISM: abundances — ISM: molecules — stars: formation

1 INTRODUCTION

Interstellar masers, such as the main-line hydroxy (OH) masers, 22-GHz water (H_2O) masers and Class II methanol (CH_3OH) masers, are one of the most readily observed signposts of star formation. These interstellar masers are powerful not only for signaling star formation regions, but also for diagnosing physical conditions (Pavlakis et al. 1996a,b), probing the kinematics of these regions (Torrelles et al. 2005; Motogi et al. 2008) and measuring trigonometric parallaxes (Xu et al. 2006a; Reid et al. 2009). Recently, with the advances of our understanding of these interstellar masers, Ellingsen et al. (2007) even recommended using them to trace different evolutionary phases of massive star formation, which may shed light on our understanding of early evolutionary stages of massive stars.

Among these species, Class II methanol masers have some advantages over H_2O and OH masers since they exclusively trace massive star-forming regions (Minier et al. 2003; Xu et al. 2008),

* Supported by the National Natural Science Foundation of China.

while H_2O and OH are known to also be associated with low mass star formation and evolved stars. To date, extensive surveys have yielded more than 800 6.7-GHz maser sites (Caswell et al. 1995; Pestalozzi et al. 2005; Pandian et al. 2007; Ellingsen 2007; Xu et al. 2008; Caswell 2009; Green et al. 2009). Recently, Purcell et al. (2009) found distinctions between radio-quiet and radio-loud subgroups of 6.7-GHz methanol masers. Wu et al. (2010, hereafter Paper I) found remarkable physical and kinematic distinctions between faint and bright subgroups of 6.7-GHz masers. Hence, there is the potential to use elaborate classifications of 6.7-GHz masers based on their associations, e.g., UCH II regions, and inherent attributes. Such applications include using maser luminosities as a clock to indicate the evolutionary stage of ongoing massive star development.

Observationally, molecular emission is a powerful tool for investigating the physical and chemical conditions in hot cores. Transitions requiring different temperatures and densities for excitation constitute an excellent probe of physical conditions. It is known that ^{12}CO is the most useful molecule tracer. When the $^{12}\text{CO}(1-0)$ lines are optically thick in most opaque regions of molecular clouds, rarer CO isotopes, i.e., ^{13}CO and C^{18}O , are usually used instead to trace the cloud's mass. In addition, HCO^+ and N_2H^+ are important ionic molecules. Determining the abundance of HCO^+ can reflect the ionization rate of clouds. Saturated and self absorbed line profiles of HCO^+ are also used to trace dynamics, like the outflow and inflow of young protostellar objects (Fuller et al. 2005; Klassen & Wilson 2007; Wu et al. 2007; Sun & Gao 2009). In contrast, N_2H^+ is an excellent tracer of quiescent high density gas (Womack et al. 1992). Moreover, since the chemical properties of hot cores vary with time, the relative molecular abundances can also be used as indicators of evolution (Bergin & Langer 1997; Langer et al. 2000). In this paper, we report our 3-mm spectral line observations, including $^{13}\text{CO}(1-0)$, $\text{C}^{18}\text{O}(1-0)$, $\text{HCO}^+(1-0)$ and $\text{N}_2\text{H}^+(1-0)$ transitions, towards a sample of nine faint 6.7-GHz methanol masers (Table 1). All nine sources have also been mapped in transitions of $\text{NH}_3(1,1)$, (2,2), (3,3) and $^{12}\text{CO}(1-0)$ in Paper I. In Section 2, we describe the sample and observations. In Section 3, we present the results which include molecular line maps and individual descriptions. Analysis is given in Section 4. Finally, conclusions are drawn in Section 5.

Table 1 List of Faint 6.7-GHz Masers

Source Name (1)	RA (J2000) (h m s) (2)	Dec (J2000) ($^\circ$ ' ") (3)	S_{peak} (Jy) (4)	V_{LSR} (km s^{-1}) (5)	D (kpc) (6)	L_{peak} (L_{\odot}) (7)	Other Name (8)	Ref. (9)
106.80+5.31	22:19:18.3	+63:18:48	0.5	-2.0	0.9^4	$7.0\text{E}-10$	S 140	13
111.25-0.77	23:16:09.7	+59:55:29	4.0	-38.5	3.5^8	$8.5\text{E}-08$	IRAS 23139+5939	12
121.24-0.34	00:36:47.358	+63:29:02.18	10	-22.8	0.85^{15}	$1.3\text{E}-08$	L 1287	9,14
133.72+1.22	02:25:41.9	+62:06:05	5	-44.5	2.3^5	$4.6\text{E}-08$	W3 IRS5	11
183.35-0.59	05:51:10.8	+25:46:14	19	-4.5	2.1^6	$1.5\text{E}-07$	IRAS 05480+2545	11
188.80+1.03	06:09:07.8	+21:50:39	4.8	-5.5	2^1	$3.3\text{E}-08$	AFGL 5182	12
189.03+0.78	06:08:40.671	+21:31:06.89	17	8.8	1.5^7	$6.6\text{E}-08$	AFGL 6466	2,14
189.78+0.34	06:08:35.28	+20:39:06.7	15	5.7	1.5^*	$5.8\text{E}-08$	S 252A	2,3
206.54-16.36	05:41:44.15	-01:54:44.9	1.48	12.4	0.415	$4.4\text{E}-10$	NGC 2024	10

Col. (1) is the source name which is named after Galactic coordinates. Cols. (2) and (3) are equatorial coordinates. Peak flux density, central velocity, distance and maser luminosity are listed in Cols. (4)–(7), respectively. Other names and references are listed in Cols. (8) and (9), respectively.

References for sources and distances:

[1] Carpenter et al. (1995); [2] Caswell et al. (1995); [3] Caswell (2009); [4] Crampton & Fisher (1974); [5] Georgelin & Georgelin (1976); [6] Hughes & Macleod (1993); [7] Humphreys (1978); [8] Larionov et al. (1999); [9] Macleod et al. (1998); [10] Minier et al. (2003); [11] Slysh et al. (1999); [12] Szymczak et al. (2000); [13] Xu et al. (2008); [14] Xu et al. (2009); [15] Yang et al. (1991);

* Heliocentric kinematic distance.

2 SAMPLE AND OBSERVATIONS

2.1 Sample

The low-luminosity 6.7-GHz methanol masers in this study were mostly selected (seven out of nine) from the catalog of Xu et al. (2003) according to their lowest luminosities (the luminosities are calculated from the peak flux density assuming a typical linewidth of 0.25 km s^{-1} and isotropic emission). Two other sources with very low luminosities, 106.80+5.31 and 206.54–16.36, were selected from Xu et al. (2008) and Minier et al. (2003) respectively. The 6.7-GHz line luminosities of these sources range from 4.4×10^{-10} to $1.5 \times 10^{-7} L_{\odot}$. Their properties, including galactic and equatorial coordinates, peak flux densities, central velocities, distances, luminosities, possible other names and references, are listed in Table 1. All of the sources have already been mapped in transitions of $\text{NH}_3(1,1)$, (2,2), (3,3) and $^{12}\text{CO}(1-0)$ in Paper I.

2.2 Observations

The observations were performed during 2008 January and 2010 March with the 13.7-m millimeter wave telescope in Delingha, China. We mapped the nine sources in transitions of $^{13}\text{CO}(1-0)$, $\text{C}^{18}\text{O}(1-0)$ and $\text{HCO}^+(1-0)$. A transition of $\text{N}_2\text{H}^+(1-0)$ was observed with a single pointing, targeted at the maser sites. A cooled SIS receiver was employed (Zuo et al. 2004), and system temperatures were $200 \sim 300 \text{ K}$ during the observations. The Acousto-Optical Spectrometer (AOS) was used to measure the transitions of $^{13}\text{CO}(1-0)$ and $\text{C}^{18}\text{O}(1-0)$ and the Fast Fourier Transform Spectrometer (FFTS) was used to measure the transitions of $\text{HCO}^+(1-0)$ and $\text{N}_2\text{H}^+(1-0)$. The HPBW was $60''$ at 110 GHz. The observations were performed in a position switched mode. The grid spacing of the mapping observations was $30''$, and the average integration time was 5 min per point. The pointing accuracy was better than $10''$. Data were calibrated using the standard chopper wheel method. S140 and NGC 2264 were used for flux calibration and observed every two hours during the observations. Absolute calibration is estimated to be accurate to about 15%. Basic information of the observations is summarized in Table 2.

Table 2 Observation Parameters

Transition	ν_{rest} (GHz)	HPBW ($''$)	Bandwidth (MHz)	$\Delta\nu_{\text{res}}$ (km s^{-1})	$1\sigma \text{ rsm}^a$ (K)
$^{13}\text{CO}(1-0)$	110.201353	60	43	0.11	0.10
$\text{C}^{18}\text{O}(1-0)$	109.782182	60	43	0.12	0.10
$\text{HCO}^+(1-0)$	89.188521	74	200	0.20	0.10
$\text{N}_2\text{H}^+(1-0)$	93.171880	71	1000	0.04	0.10

Notes: ^a typical value in the scale of brightness temperature for the reduced spectra.

Data were processed using the CLASS and GREG packages of GILDAS¹ software, including baseline subtraction, fitting Gaussian line profiles and hyperfine structure fitting (HFS) of $\text{N}_2\text{H}^+(1-0)$ lines.

3 RESULTS

N_2H^+ emission is detected in six sources, C^{18}O emission is detected in eight sources, and ^{13}CO and HCO^+ are detected in all sources. Detected spectral lines are at least $3\text{-}\sigma$ above the baseline and in

¹ CLASS and GREG are part of the Grenoble Image and Line Data Analysis Software (GILDAS) working group's software. <http://www.iram.fr/IRAMFR/GILDAS/>

Table 3 Detection Rates of Molecular Lines

Source Name	$^{13}\text{CO}(1-0)$	$\text{C}^{18}\text{O}(1-0)$	$\text{HCO}^+(1-0)$	$\text{N}_2\text{H}^+(1-0)$
106.80+5.31	Y	Y	Y	Y
111.25-0.77	Y	Y	Y	N
121.24-0.34	Y	Y	Y	Y
133.72+1.22	Y	N	Y	N
183.35-0.59	Y	Y	Y	Y
188.80+1.03	Y	Y	Y	N
189.03+0.78	Y	Y	Y	Y
189.78+0.34	Y	Y	Y	Y
206.54-16.3	Y	Y	Y	Y
Detection Rate	9/9	8/9	9/9	6/9

Notes: “Y” indicates detection, “N” indicates no detection.

most cases have a signal to noise ratio greater than five. The detailed detections for individual sources are presented in Table 3. Recently, similar 3-mm spectral line surveys towards southern 6.7-GHz methanol masers presented high detection rates (99%) of $\text{HCO}^+(1-0)$, $\text{N}_2\text{H}^+(1-0)$ and $^{13}\text{CO}(1-0)$ (Purcell et al. 2009). Our detection rates of $^{13}\text{CO}(1-0)$ and $\text{HCO}^+(1-0)$ are 100%, similar to the 99% detection rates of Purcell et al. (2009), while our detection rate of $\text{N}_2\text{H}^+(1-0)$ is 66%, lower than the 99% rate of Purcell et al. (2009). The lower detection rate of $\text{N}_2\text{H}^+(1-0)$ may be due to the relatively lower sensitivity of our observations.

3.1 Spectra

In Figure 1, we present the $^{13}\text{CO}(1-0)$, $\text{C}^{18}\text{O}(1-0)$, $\text{HCO}^+(1-0)$ and $\text{N}_2\text{H}^+(1-0)$ spectra at the positions of the peak of the maser associated cores. $^{13}\text{CO}(1-0)$, $\text{C}^{18}\text{O}(1-0)$, and $\text{HCO}^+(1-0)$ lines are fitted with Gaussian profiles. For $\text{HCO}^+(1-0)$ spectra with evidence of self absorption, though exhibiting a double-peak profile, are fitted with a single Gaussian function. Spectral parameters, i.e., bright temperatures, line width, velocity of the local standard of rest (V_{LSR}), and integral intensities of $^{13}\text{CO}(1-0)$, $\text{C}^{18}\text{O}(1-0)$, and $\text{HCO}^+(1-0)$, are listed in Table 4. For $\text{N}_2\text{H}^+(1-0)$, following Purcell et al. (2009), we fit the spectra with two methods: (1) the hyperfine structure fitting routine in the CLASS software, considering the seven-component structure; (2) three-Gaussian fitting of the three blended groups. The fitted parameters of both methods are presented in Table 5.

3.2 Maps

Contours of $^{13}\text{CO}(1-0)$, $\text{C}^{18}\text{O}(1-0)$ and $\text{HCO}^+(1-0)$ integrated intensities are presented in Figure 2. We use infrared dust emission, from the Midcourse Space Experiment (MSX) E band ($21\ \mu\text{m}$) images, as the background for the contours. For 106.80+5.31, where no MSX data are available, the Multiband Imaging Photometer for Spitzer (MIPS) $24\ \mu\text{m}$ image is used. The central blank pixels in the $24\ \mu\text{m}$ image are due to saturation. The squares, triangles, pluses and ellipses in Figure 2 denote the 6.7-GHz CH_3OH masers, H_2O masers, OH masers and error ellipses of the IRAS point sources in the fields, respectively. We use $\text{C}^{18}\text{O}(1-0)$ (optical thin line) contours to define a concentrated structure, i.e., a core, and determine the size and position of the core. Although for 133.72+1.22 where there is no detection of C^{18}O , the cores are identified from the ^{13}CO map and core 1 of 189.78+0.34, where there is no C^{18}O emission peak, is identified from the HCO^+ map. Cores were identified using visual inspection. The methodology used to define cores is similar to the operation of the “CLUMPFIND” algorithm (Williams et al. 1994). Totally, we find 17 cores from the nine fields, with eight cores showing no maser associations.

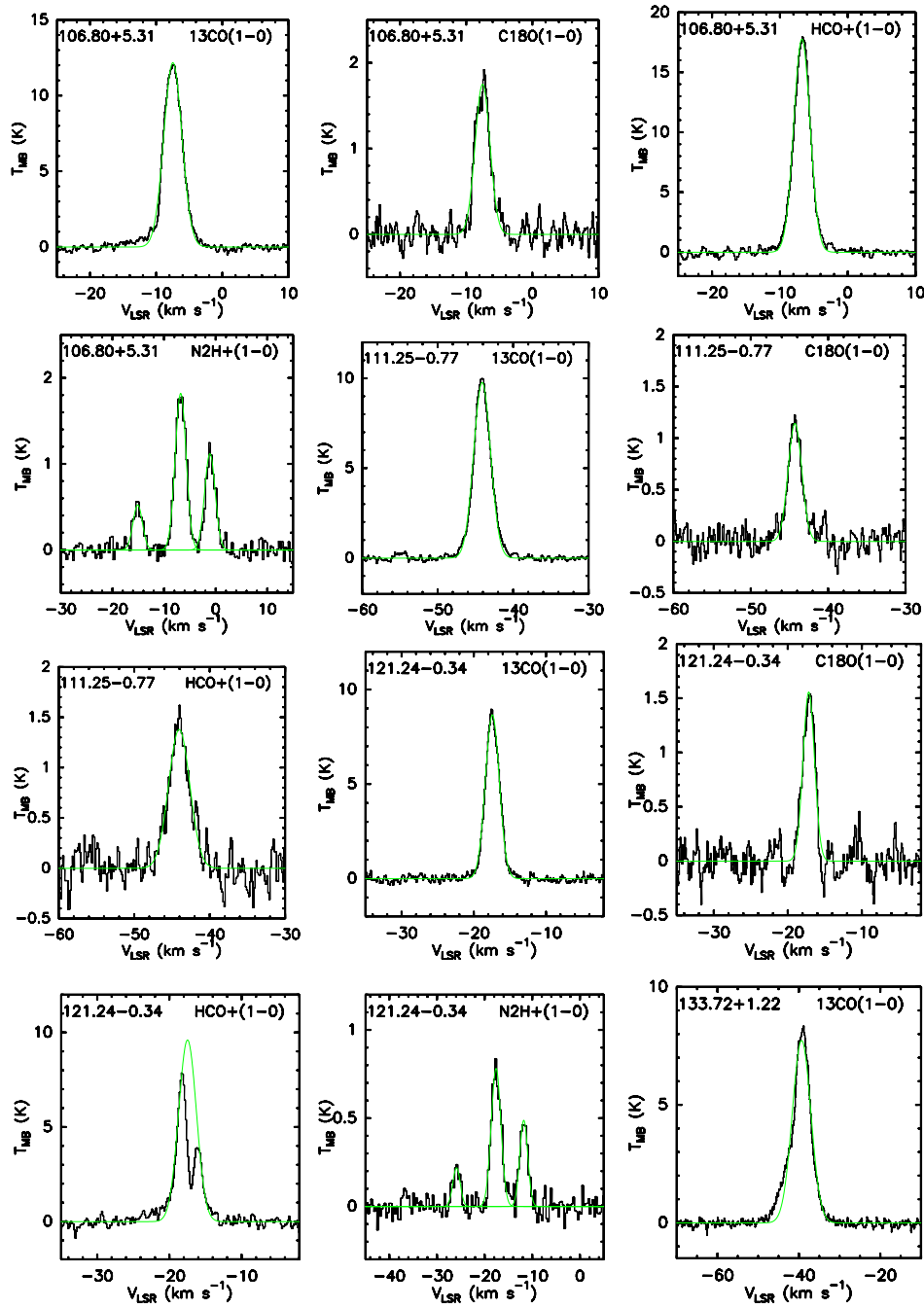
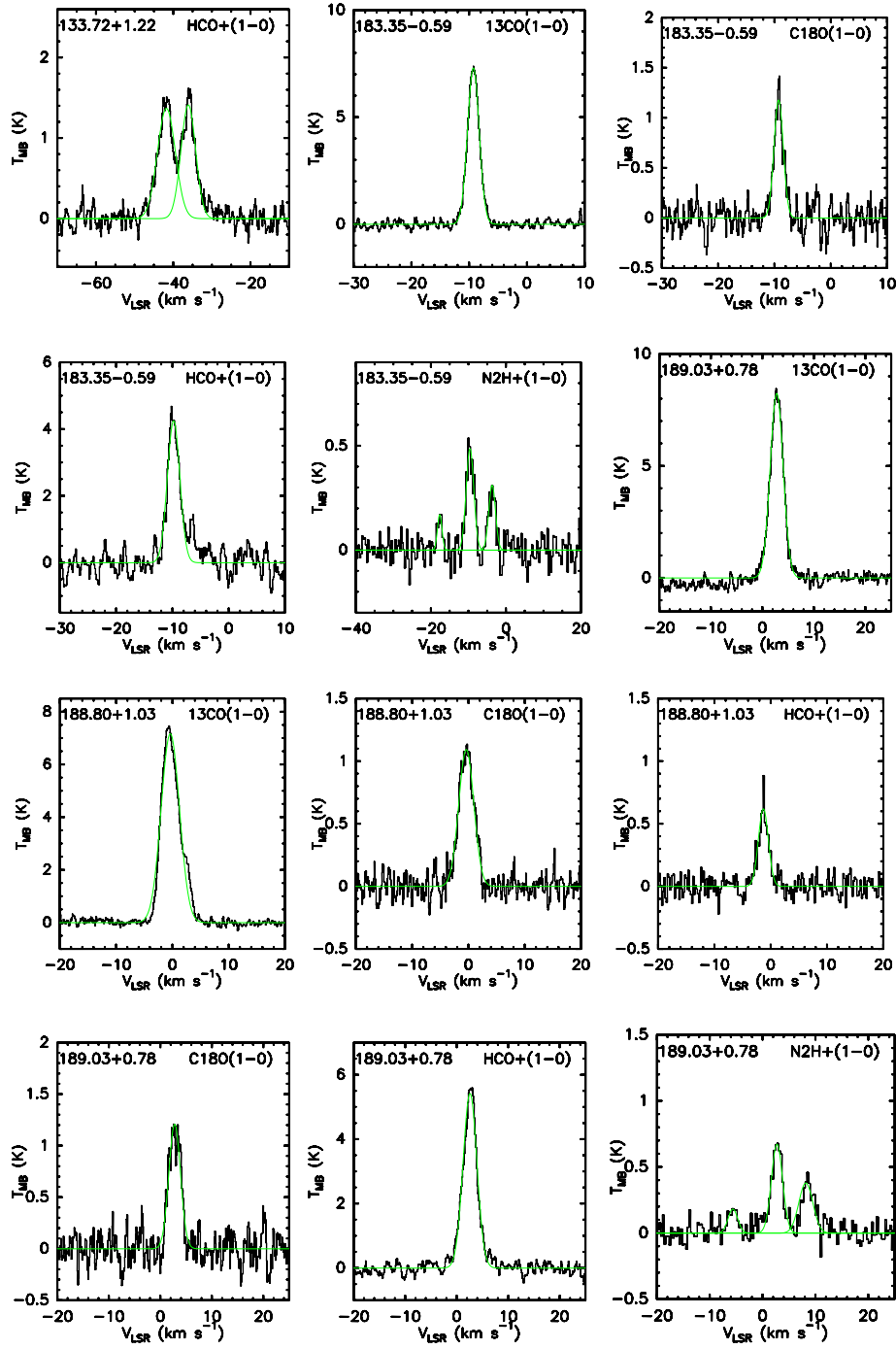
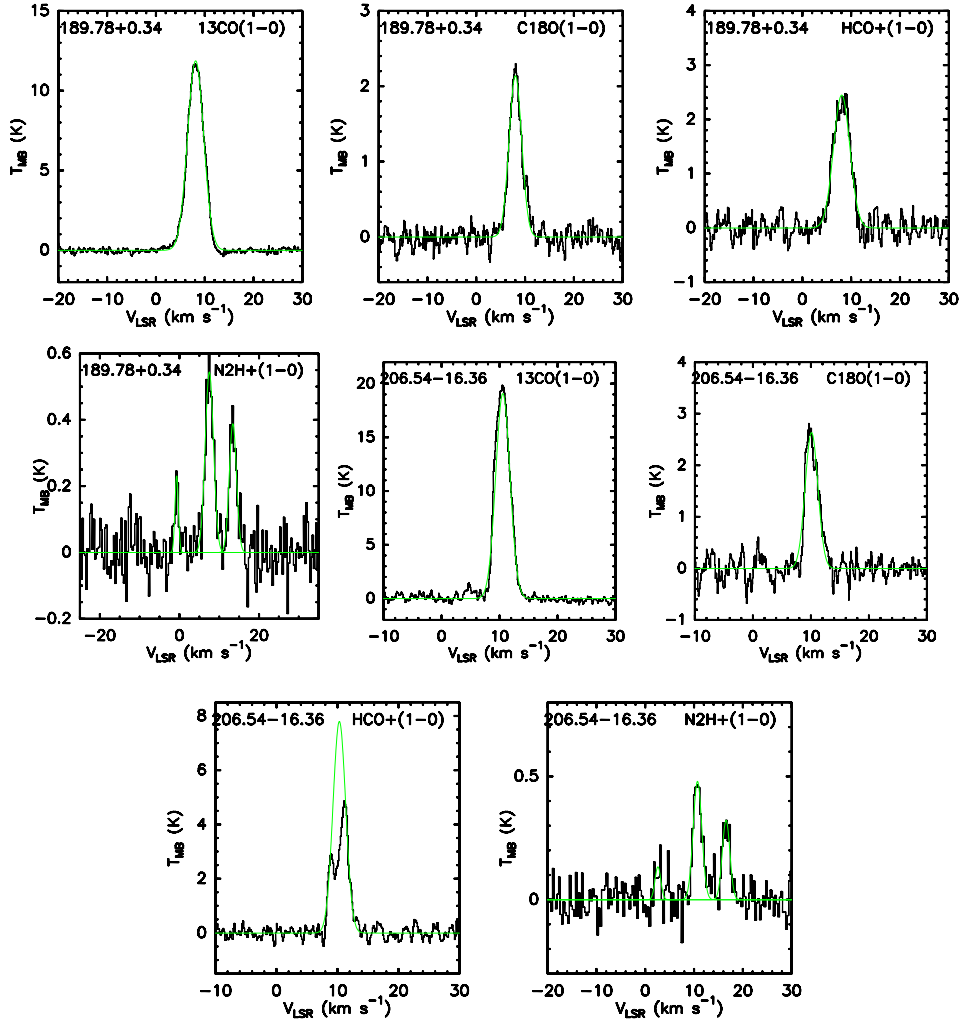


Fig. 1 $^{13}\text{CO}(1-0)$, $\text{C}^{18}\text{O}(1-0)$, $\text{HCO}^+(1-0)$ and $\text{N}_2\text{H}^+(1-0)$ spectra at the positions of the peak of the maser associated cores. The velocities are the radial velocity with respect to the local standard of rest. The y -axis is the main beam temperature (green lines are fitted profiles, color online).

Fig. 1 — *Continued.*

Fig. 1 — *Continued.*

3.3 Comments on Individual Sources

- 106.80+5.31 — This source is located in the central part of the S140 molecular complex. Both the $^{13}\text{CO}(1-0)$ and $\text{C}^{18}\text{O}(1-0)$ maps show a filamented structure extending southwest to northeast and peak at the central infrared source. The HCO^+ map reveals a single core surrounding the central infrared source. All the three maser species, i.e., CH_3OH , H_2O and OH masers, were found in this region.
- 111.25–0.77 — There is a single core peak towards the IRAS 23139+5939. The ^{13}CO maps reveal an extended emission elongating towards the northern direction. Both H_2O and CH_3OH masers were found in this region.
- 121.24–0.34 — There is a single core which elongates northwest to southeast and peaks at IRAS 00338+6312. Both H_2O and CH_3OH masers were found in this region.
- 133.72+1.22 — This is an intensively studied region of active star formation, the W3 complex. $^{13}\text{CO}(1-0)$ and $\text{HCO}^+(1-0)$ spectra show two velocity components, with velocity ranges of

- 48~–42 km s⁻¹ and –40~–36 km s⁻¹, respectively. In the ¹³CO integrated intensity map with a velocity range of –48~–42 km s⁻¹, one can see a two-core structure, with the eastern core (Core 1) peaking towards the CH₃OH maser and the western core (Core 2) associated with the western mid-infrared dust core. In the ¹³CO integrated intensity map with a velocity range of –40~–36 km s⁻¹, there is a filament consisting of two cores, with the northwestern core (Core 3) departing ~ 30'' south of IRAS 02219+6152 and the southeastern core (Core 4) departing ~ 2' southeast of the IRAS source. Emission of HCO⁺ shows a similar distribution. Three H₂O and one CH₃OH masers are found in this field.
- 183.35–0.59 — A single core is located southwest and with an offset of ~ 15'' from IRAS 05480+2545. Only the CH₃OH maser is found in this region.
 - 188.80+1.03 — Both C¹⁸O(1–0) and HCO⁺ maps reveal a filament consisting of two cores which extend southwest to northeast through the field. Core 1 (the southeast core) is offset by ~ 30'' southeast towards IRAS source 06061+2151 and Core 2 (the northwest core) is offset by ~ 30'' northeast towards the IRAS source. H₂O and CH₃OH masers are found in this region.
 - 189.03+0.78 — The mid-infrared dust emission of this region shows two heat sources. Emission of CO and HCO⁺ reveals a filament extending from the southwest infrared source towards the northeast one. The filament in the C¹⁸O map consists of two cores. The southwestern core (Core 1) is associated with IRAS 06056+2131. The northeastern core (Core 2) is located in the middle of the two mid-infrared cores departing ~ 1' northeast towards IRAS 06056+2131. Both H₂O and CH₃OH masers are found to be associated with Core 1.
 - 189.78+0.34 — This source is part of the S252A molecular complex. ¹³CO and C¹⁸O maps reveal a filamented structure consisting of two cores and extending from north to south, while the HCO⁺ map presents a filament extending northwest to southeast and peaking towards the CH₃OH maser.
 - 206.54–16.36 — It is located in the vicinity of the NGC 2024 HII region. A filament, called the “Molecular Ridge,” is elongated in the north-south direction (Chandler & Carlstrom 1996). The filament is segregated into two segments on the C¹⁸O maps. Along the ridge, there are seven far infrared sources (Mezger et al. 1988, 1992). The CH₃OH maser is associated with FIR4 (Minier et al. 2003).

Table 4 ¹³CO(1–0), C¹⁸O(1–0), and HCO⁺(1–0) spectral parameters, including bright temperatures, integrated intensities, central velocities and fitted line widths.

Region	Core ^α	¹³ CO				C ¹⁸ O				HCO ⁺			
		T_R^* (K)	$\int T_R^* dV$ (K km s ⁻¹)	V_{LSR} (km s ⁻¹)	ΔV (km s ⁻¹)	T_R^* (K)	$\int T_R^* dV$ (K km s ⁻¹)	V_{LSR} (km s ⁻¹)	ΔV (km s ⁻¹)	T_R^* (K)	$\int T_R^* dV$ (K km s ⁻¹)	V_{LSR} (km s ⁻¹)	ΔV (km s ⁻¹)
106.80+5.31	1	12.22	42.34	-7.46(01)	3.26(02)	1.85	5.73	-7.52(04)	2.91(11)	17.82	53.71	-6.74(01)	2.83(02)
111.25–0.77	1	9.78	27.43	-44.09(01)	2.64(03)	1.14	2.49	-44.28(04)	2.05(11)	1.37	4.79	-44.02(05)	3.27(14)
121.24–0.34	1	9.06	21.46	-17.39(01)	2.22(03)	1.57	3.11	-17.15(04)	1.87(08)	8.70	27.75	-17.53(02)	3.00(06)
133.72+1.22	1	8.35	29.18	—	—	—	—	—	—	1.81	9.52	-40.57(05)	4.91(14)
133.72+1.22	2	5.67	29.75	-43.37(01)	4.93(03)	—	—	—	—	1.41	7.39	-41.89(05)	4.91(14)
133.72+1.22	3	8.17	46.05	-38.88(03)	5.40(02)	—	—	—	—	1.40	7.00	-36.14(05)	4.71(14)
133.72+1.22	4	9.06	28.15	-38.88(02)	2.92(02)	—	—	—	—	1.38	4.14	-39.50(05)	2.81(15)
183.35–0.59	1	7.30	18.44	-9.25(01)	2.37(02)	1.16	2.34	-9.24(04)	1.90(10)	4.25	12.17	-9.76(05)	2.69(15)
188.80+1.03	1	6.99	20.63	-0.58(01)	2.77(02)	1.00	2.83	-0.39(06)	2.65(15)	0.68	1.81	-1.25(06)	2.54(16)
188.80+1.03	2	6.96	21.90	-0.17(01)	2.96(02)	1.35	2.97	-0.41(02)	2.08(05)	0.66	1.99	-1.15(07)	2.83(16)
189.03+0.78	1	8.31	26.70	2.79(01)	3.02(02)	1.26	3.66	2.81(06)	2.74(13)	5.44	18.47	2.59(01)	3.19(04)
189.03+0.78	2	8.56	24.27	2.32(01)	2.66(03)	1.63	3.82	2.13(03)	2.20(09)	3.06	10.19	2.28(35)	3.12(09)
189.78+0.34	1	12.26	41.28	8.64(01)	3.16(02)	2.21	4.81	8.55(02)	2.24(05)	2.77	13.52	7.99(04)	4.58(09)
189.78+0.34	2	11.89	49.23	8.15(01)	3.89(01)	2.39	7.18	8.04(02)	3.03(05)	2.05	8.32	7.70(05)	3.83(13)
189.78+0.34	3	10.92	45.76	8.31(01)	3.94(01)	2.68	5.09	7.67(02)	1.96(07)	1.39	5.83	7.78(08)	3.94(19)
206.54–16.36	1	20.43	57.08	10.33(01)	2.68(01)	3.81	7.49	10.04(02)	1.94(06)	3.47	10.97	10.06(03)	2.66(09)
206.54–16.36	2	21.27	66.54	10.61(01)	2.94(02)	3.17	9.48	10.28(02)	2.81(04)	4.45	17.54	10.72(04)	3.70(07)

Notes: α: 1, 2, 3, and 4 denote the different components in the same field.

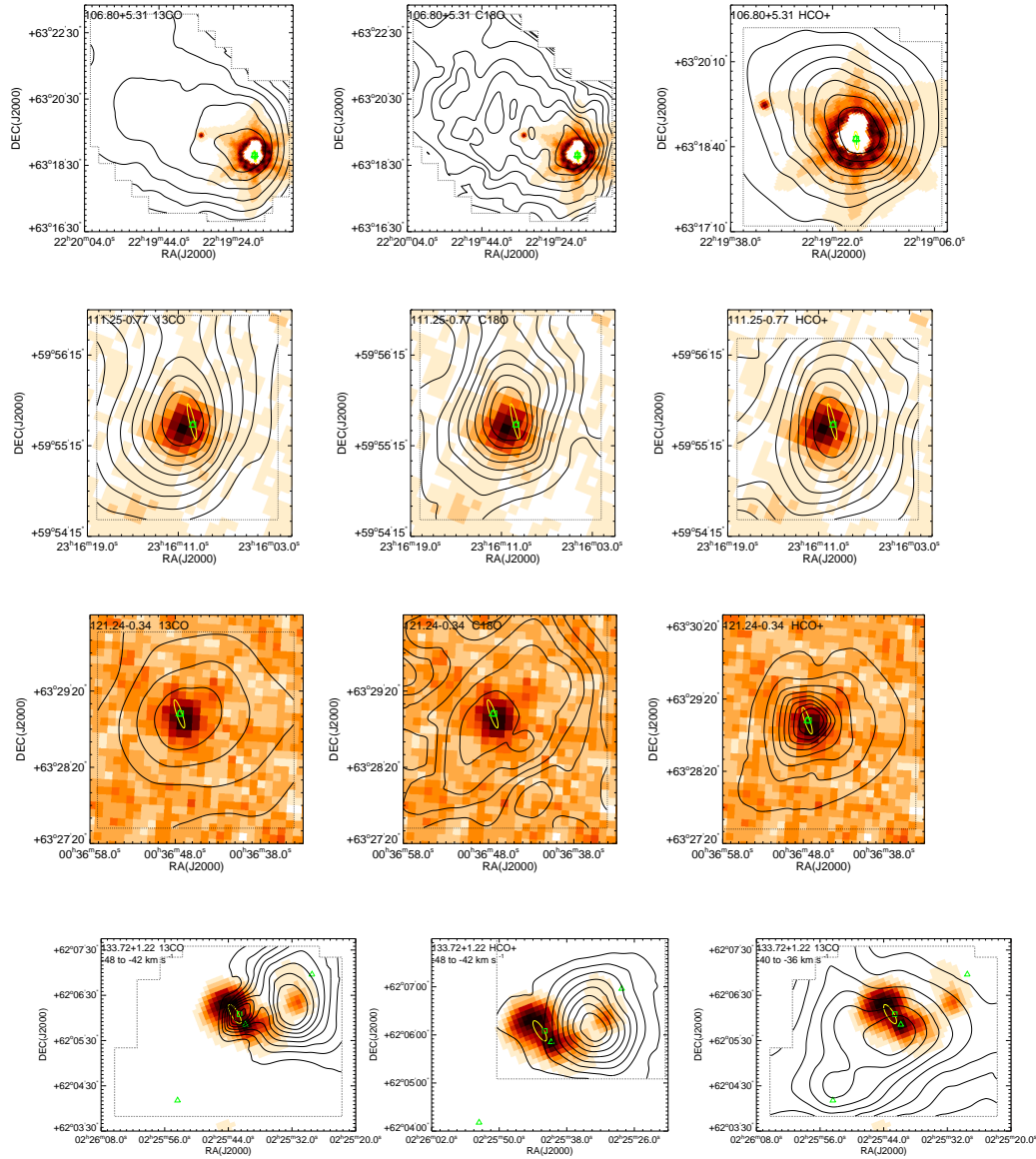


Fig. 2 $^{13}\text{CO}(1-0)$, $\text{C}^{18}\text{O}(1-0)$ and $\text{HCO}^+(1-0)$ maps of faint maser regions. The grey scale images are MSX $21\ \mu\text{m}$ images except for 106.80+5.31, where the grey scale image is the MIPS $24\ \mu\text{m}$ image. The central blank pixels in the $24\ \mu\text{m}$ image are due to saturation. The squares, triangles, crosses and ellipses denote the CH_3OH masers, H_2O masers, OH masers and error ellipses of the IRAS point sources in the fields, respectively. The contours are chosen to highlight the most prominent features in each source, usually between 20% and 90% (steps of 10%) of the peak integrated intensity. The thicker lines denote the 50% levels of the peak integrated intensity which are used to determine the core sizes.

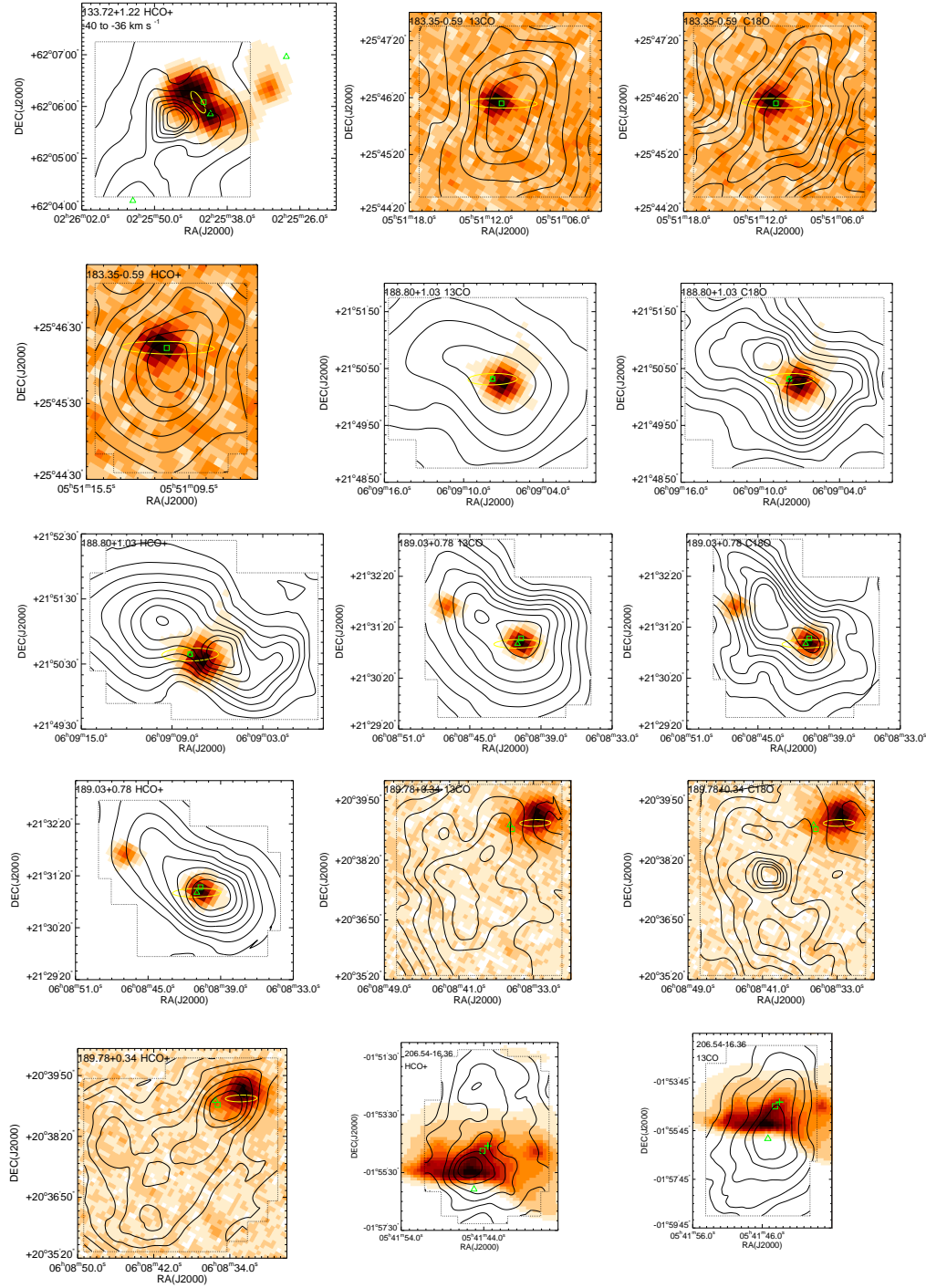


Fig. 2 — Continued.

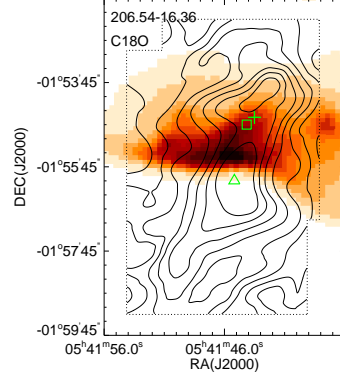


Fig. 2 — *Continued.*

3.4 Physical Quantities

3.4.1 Optical depth and excitation temperature

In this section, we derive optical depths and excitation temperatures of CO and N_2H^+ transitions. For ^{13}CO and C^{18}O , the optical depths and excitation temperatures are estimated by assuming $^{12}\text{CO}(1-0)$ lines are optically thick with formulae 1–3 of Wu et al. (2009). For N_2H^+ , due to the uncertainty introduced by the blended profiles, optical depths of N_2H^+ cannot be directly fitted with the HFS routine, but rather can be derived from the ratio of integrated intensities, $\int T_B dv$, of the three blended groups with a method of Purcell et al. (2009), using equation

$$\frac{\int T_{B,1} dv}{\int T_{B,2} dv} = \frac{1 - e^{-\tau_1}}{1 - e^{-\tau_2}} = \frac{1 - e^{-\tau_1}}{1 - e^{-a\tau_1}}, \quad (1)$$

where ‘a’ is the expected ratio of τ_2/τ_1 , which should be 1:5:2 under optically thin conditions. It is noted that the optical depth derived here is the “group optical depth” that contains contributions of (21–12), (23–12) and (22–11) components.

Table 5 Fitted Profile Parameters for N_2H^+

Source	7-component HFS fits α		3-Gaussian fits γ					
	V_{LSR}^β (km s^{-1})	ΔV (km s^{-1})	Group-1		Group-2		Group-3	
			$\int T_R^* dV$ (K km s^{-1})	ΔV (km s^{-1})	$\int T_R^* dV$ (K km s^{-1})	ΔV (km s^{-1})	$\int T_R^* dV$ (K km s^{-1})	ΔV (km s^{-1})
106.80+5.31	-6.95(02)	1.71(05)	1.20	2.15(19)	4.82	2.48(20)	2.87	2.41(39)
121.24-0.34	-17.75(03)	1.56(07)	0.43	1.84(24)	1.99	2.39(19)	1.02	1.96(24)
183.35-0.59	-9.70(06)	1.60(11)	0.26	1.41(30)	1.24	2.39(20)	0.70	2.11(34)
189.03+0.78	2.58(06)	1.85(13)	0.40	2.01(46)	1.79	2.50(30)	1.27	3.14(17)
189.78+0.34	7.44(06)	1.55(15)	0.23	0.94(34)	1.43	2.47(28)	1.22	2.93(74)
206.54-16.36	10.62(06)	1.30(12)	—	—	1.07	2.09(25)	0.63	1.82(23)

Notes: α : fitted with the CLASS HFS routine considering the 7-component structure;

β : V_{LSR} is referring to the $F_1, F = 2, 3 \rightarrow 1, 2$ transition, i.e. the center component of ‘Group-2’;

γ : Gaussian fits to the three groups.

Then we derived (23–12) excitation temperatures of $\text{N}_2\text{H}^+(1-0)$ using equation

$$T_R = T_o \left[\frac{1}{e^{T_o/T_{\text{ex}}} - 1} - \frac{1}{e^{T_o/T_{\text{bg}}} - 1} \right] (1 - e^{-\tau}), \quad (2)$$

where T_R and τ are brightness temperature and optical depth for the (23–12) component, $T_o = h\nu/k$, and $T_{\text{bg}} = 2.7$ K.

The optical depths and excitation temperatures of ^{13}CO , C^{18}O and N_2H^+ are tabulated in Table 6. The typical optical depths are 0.7, 0.08 and 0.3 for ^{13}CO , C^{18}O and N_2H^+ , respectively. CO excitation temperatures range from 15 K to 48 K, with a mean value of 28 K. Excitation temperatures for N_2H^+ range from 5 K to 12 K, with a mean value of 7 K. Since the calculations are based on a uniform beam filling factor, the excitation temperatures (especially for N_2H^+) derived here should be the lower limits of the true values.

Table 6 Optical Depths, Column Densities and Abundances

Region	Core	Optical Depth τ			Excitation Temperature		Column Density N			Abundance γ	
		^{13}CO	C^{18}O	N_2H^+	α	$T_{\text{ex}}(\text{CO})$ (K)	$T_{\text{ex}}(\text{N}_2\text{H}^+)^{\beta}$ (K)	^{13}CO (cm^{-2})	C^{18}O (cm^{-2})	N_2H^+ 10^{12}cm^{-2}	$X(\text{C}^{18}\text{O})$ 10^{-7}
106.80+5.31	1	0.62	0.08	0.30	32.8(4.9)	12.1(2.9)	9.50E+16	1.01E+16	8.96	2.12	1.89E–10
111.25–0.77	1	0.85	0.07	—	23.8(3.6)	—	5.09E+16	3.26E+15	—	1.28	—
121.24–0.34	1	0.80	0.10	0.27	22.0(3.3)	7.4(2.7)	3.63E+16	3.85E+15	2.48	2.12	1.37E–10
133.72+1.22	1	0.31	—	—	35.0(5.7)	—	6.01E+16	—	—	—	—
133.72+1.22	2	0.24	—	—	38.3(5.7)	—	6.46E+16	—	—	—	—
133.72+1.22	3	0.33	—	—	32.3(4.8)	—	8.60E+16	—	—	—	—
133.72+1.22	4	0.49	—	—	27.7(4.5)	—	5.14E+16	—	—	—	—
183.35–0.59	1	1.02	0.13	0.32	21.2(3.2)	5.1(3.1)	3.32E+16	2.85E+15	1.23	1.72	7.42E–11
188.80+1.03	1	0.69	0.07	—	20.7(3.1)	—	3.15E+16	3.27E+15	—	2.08	—
188.80+1.03	2	1.23	0.17	—	14.6(2.2)	—	3.12E+16	2.68E+15	—	1.72	—
189.03+0.78	1	0.72	0.08	0.25	23.1(3.5)	7.3(6.3)	4.56E+16	4.69E+15	2.19	2.06	9.62E–11
189.03+0.78	2	0.89	0.14	—	17.2(2.6)	—	3.45E+16	3.89E+15	—	2.26	—
189.78+0.34	1	0.72	0.09	0.37	33.1(4.9)	5.0(2.3)	9.76E+16	8.58E+15	1.44	1.76	2.94E–11
189.78+0.34	2	0.82	0.13	—	29.1(4.4)	—	1.08E+17	1.16E+16	—	2.15	—
189.78+0.34	3	0.76	0.16	—	27.1(4.1)	—	9.17E+16	7.82E+15	—	1.71	—
206.54–16.36	1	0.94	0.09	0.33	36.0(5.4)	5.0(4.3)	1.60E+17	1.44E+16	1.05	1.80	1.31E–11
206.54–16.36	2	1.54	0.13	—	36.7(5.5)	—	2.42E+17	1.90E+16	—	1.57	—
mean $^{\delta}$	—	0.74	0.09	0.31	27.52	6.97	6.78E+16	6.37E+15	2.89	1.87	8.98E–11
median	—	0.72	0.09	0.31	23.80	6.20	5.09E+16	4.27E+15	1.83	1.93	8.52E–11

α : $\tau(\text{N}_2\text{H}^+)$ is the “group optical depth” that contains contributions of (21–12), (23–12) and (22–11) components;

β : $T_{\text{ex}}(\text{N}_2\text{H}^+)$ is (23–12) excitation temperature;

γ : the abundances were derived with the assumption of $X(^{13}\text{CO}) \sim 2 \times 10^{-6}$;

δ : mean and median values are only for cores associated with masers, i.e., Core 1.

3.4.2 Column density and chemical abundance

With optical depths and excitation temperatures, total column densities of ^{13}CO , C^{18}O and N_2H^+ can be obtained from (eq. (A1), Scoville et al. 1986)

$$N = \frac{3k}{8\pi^3 B\mu^2} \frac{\exp[hBJ_l(J_l+1)/kT_{\text{ex}}]}{(J_l+1)} \frac{T_{\text{ex}} + hB/3k}{1 - \exp[-h\nu/kT_{\text{ex}}]} \int \tau dv, \quad (3)$$

where B is the rotational constant of the molecule and μ is the permanent dipole moment of the molecule. The values of B and μ are taken to be 55.101 MHz and 0.1098 Debye for ^{13}CO , 54.891

MHz and 0.1098 Debye for $C^{18}O$ (Lovas & Krupenie 1974), and 46.587 MHz and 3.37 Debye for N_2H^+ (Botschwina 1984). J_l is the rotational quantum number of the lower state in the observed transitions. Column densities of ^{13}CO , $C^{18}O$ and N_2H^+ are presented in Table 6. Typical column densities of ^{13}CO , $C^{18}O$ and N_2H^+ are 5×10^{16} , 4×10^{15} and 1×10^{12} cm^{-2} , respectively. For HCO^+ , whose excitation temperature and optical depth are lacking, we are unable to calculate reliable column densities. It is noted that the column densities, especially for N_2H^+ , estimated here should be the lower limits, because of the underestimate of excitation temperatures. The total N_2H^+ column density calculated with an excitation temperature of 20 K should be three times larger than the value estimated with an excitation temperature of 5 K.

The relative abundance X between two species may be found directly from the ratio of their volume densities. Assuming both molecules occupy the same volume of space, the ratio of two species $X = n_1/n_2 \approx N_1/N_2$. Recently, the COMPLETE molecular survey gave an estimated value of $[H_2/^{13}CO]$ in the range of 2.8 to 4.9×10^5 (Pineda et al. 2008). The chemical evolution model suggested a more stable CO abundance relative to HCO^+ and N_2H^+ (Bergin & Langer 1997). Thus, assuming a moderate ^{13}CO abundance of 3×10^{-6} , we derived the molecular abundances of $C^{18}O$ and N_2H^+ for the targeted low-luminosity 6.7-GHz maser regions. The results of column densities and chemical abundances are presented in Table 6.

The abundances of $C^{18}O$ range from 1.3 to 2.3×10^{-7} , with a median value of 1.9×10^{-7} , but the abundances of N_2H^+ range from 1.3×10^{-11} to 1.9×10^{-10} , with a median value of 8.5×10^{-11} . In contrast, the abundance fluctuation of N_2H^+ is more dramatic than that of $C^{18}O$.

3.4.3 Core size and mass

The nominal core sizes, l , were determined from contours of the $C^{18}O$ integral intensities by deconvolving the telescope beam, using Equation (4),

$$l = D \left(\theta_{1/2}^2 - \theta_{MB}^2 \right)^{1/2}, \quad (4)$$

where D is the distance, $\theta_{1/2}$ is the half-power angular size of the core, and θ_{MB} is the half-power beam width of the telescope.

Core masses were computed by assuming a Gaussian column density distribution with a full-width at half-maximum (FWHM) of l . If $N(H_2)$ is the molecular hydrogen column density of the peak position, m_{H_2} is the mass of a hydrogen molecule and μ is the ratio of total gas mass to hydrogen mass (assumed to be 1.36 based on Hildebrand 1983), the core mass is given by

$$M_{\text{gas}} \simeq \mu m_{H_2} \int 2\pi r N(H_2) e^{-4 \ln 2 (r/l)^2} dr. \quad (5)$$

With linewidths and core sizes, we also estimated the virial masses following the approach by MacLaren et al. (1988)

$$M_{\text{vir}} = 126r \Delta v^2, \quad (6)$$

where r is the radius of the core in pc, Δv is the FWHM linewidth of $C^{18}O$ in $km\ s^{-1}$ and M_{vir} is the virial mass in M_{\odot} .

The estimated nominal core sizes, gas masses and virial masses are tabulated in Table 7.

4 DISCUSSION

4.1 Line Profiles

Line profiles of ^{13}CO and $C^{18}O$ are relatively simple and can be well fitted with a single Gaussian. In Figure 3 we present example spectra for the source 121.24–0.34 alongside the $^{13}CO(1-0)$ contour.

Table 7 Physical Quantities of the Cores

Region Name (1)	Core (2)	R.A. (h m s) (3)	Dec. ($^{\circ}$ ' ") (4)	Angular (", ") (5)	Size (pc) (6)	$N(\text{H}_2)$ ($\times 10^{22} \text{ cm}^{-2}$) (7)	M_{gas} (M_{\odot}) (8)	M_{vir} (M_{\odot}) (9)
106.80+5.31	1	22:19:20.0	+63:19:10	(120, 90)	0.33	4.75	134	88
111.25-0.77	1	23:16:10.0	+59:55:30	(70, 60)	0.37	2.55	91	49
121.24-0.34	1	00:36:47.8	+63:28:57	(110, 70)	0.23	1.82	25	25
133.72+1.22	1	02:25:41.8	+62:06:05	(30, 30)	0.29	3.01	66	220
133.72+1.22	2	02:25:32.0	+62:06:22	(120, 90)	0.84	3.23	592	638
133.72+1.22	3	02:25:41.8	+62:05:40	(150, 90)	0.98	4.30	1073	685
133.72+1.22	4	02:25:53.5	+62:04:35	(90, 60)	0.42	2.57	118	105
183.35-0.59	1	05:51:10.5	+25:46:05	(120, 90)	0.76	1.66	249	86
188.80+1.03	1	06:09:06.5	+21:50:20	(90, 70)	0.45	1.58	83	100
188.80+1.03	2	06:09:09.4	+21:51:06	(75, 70)	0.35	1.56	50	48
189.03+0.78	1	06:08:41.0	+21:31:08	(70, 70)	0.23	2.28	31	54
189.03+0.78	2	06:08:44.5	+21:31:40	(90, 60)	0.27	1.73	33	41
189.78+0.34	1	06:08:34.5	+20:39:00	(100, 80)	0.43	4.88	235	68
189.78+0.34	2	06:08:40.5	+20:38:00	(90, 60)	0.27	5.40	102	78
189.78+0.34	3	06:08:40.5	+20:36:30	(90, 60)	0.27	4.59	87	33
206.54-16.36	1	05:41:43.5	-01:54:05	(90, 80)	0.11	8.00	25	13
206.54-16.36	2	05:41:45.0	-01:56:05	(120, 100)	0.16	12.10	81	40
Mean	—	—	—	—	0.36	3.39	104	78
Median	—	—	—	—	0.33	2.55	83	68

Cols. (3) and (4) are equatorial coordinates, Col. (5) is angular extensions of the major and minor axes of the core assuming a spherical geometry. Col. (6) is the nominal core size. Col. (7) is molecular hydrogen column density, $N(\text{H}_2)$. Gas masses and virial masses are listed in Cols. (8)–(9), respectively. Mean and median values of these quantities are listed in the last two rows.

The spectrum of N_2H^+ is fitted with the HFS routine in the CLASS software to simultaneously fit the N_2H^+ profiles with seven Gaussian distributions. In case of a cold quiescent environment, e.g., a dark cloud, the spectrum of $\text{N}_2\text{H}^+(1-0)$ can exhibit seven hyperfine components (Womack et al. 1992). In our case, however, the seven components of N_2H^+ are blended into three groups due to large linewidths.

In Figure 3, the spectrum of HCO^+ exhibits a double-peak profile. By contrast, the spectrum of C^{18}O , an optically thin line, shows a single peak located at the dip of HCO^+ , which indicates that the double-peak profile of $\text{HCO}^+(1-0)$ is a self-absorption feature. Therefore, we fit the HCO^+ spectrum with a single Gaussian by blanking the absorption dip. This “blue profile” is considered as a signature of inflow. Wu et al. (2007) conducted an HCO^+ survey towards high mass star forming regions and obtained a high rate of incidence for this kind of “blue profile” (29%). However, in our sample, this inflow signature is only found towards 121.24–0.34, corresponding to a rate of 11%. In addition, the self-absorption feature is also found in the HCO^+ spectrum of 206.54–16.36, but in contrast to 121.24–0.34, the HCO^+ spectrum of 206.54–16.36 shows an excess of the red profile which may be evidence of expansion. Emprechtinger et al. (2009) established a sophisticated model based on the scenario of a PDR and the “Blister model” to interpret the complex line shapes of the multiple CO transition from 206.54–16.36.

Figure 4 shows the linewidth of the four molecules as an function of maser luminosity. The mean linewidths towards these low-luminosity maser regions are as follows: HCO^+ : 3.3 km s^{-1} , ^{13}CO : 2.8 km s^{-1} , C^{18}O : 2.3 km s^{-1} and N_2H^+ : 1.6 km s^{-1} . In general, linewidths of HCO^+ are larger than ^{13}CO , C^{18}O and N_2H^+ . Purcell et al. (2006, 2009) surveyed 83 southern methanol masers and obtained larger mean linewidths: HCO^+ : 5.1 km s^{-1} , ^{13}CO : 4.8 km s^{-1} , and N_2H^+ : 3.0 km s^{-1} . It is obvious that linewidths in our sample, including only low-luminosity masers, are smaller than

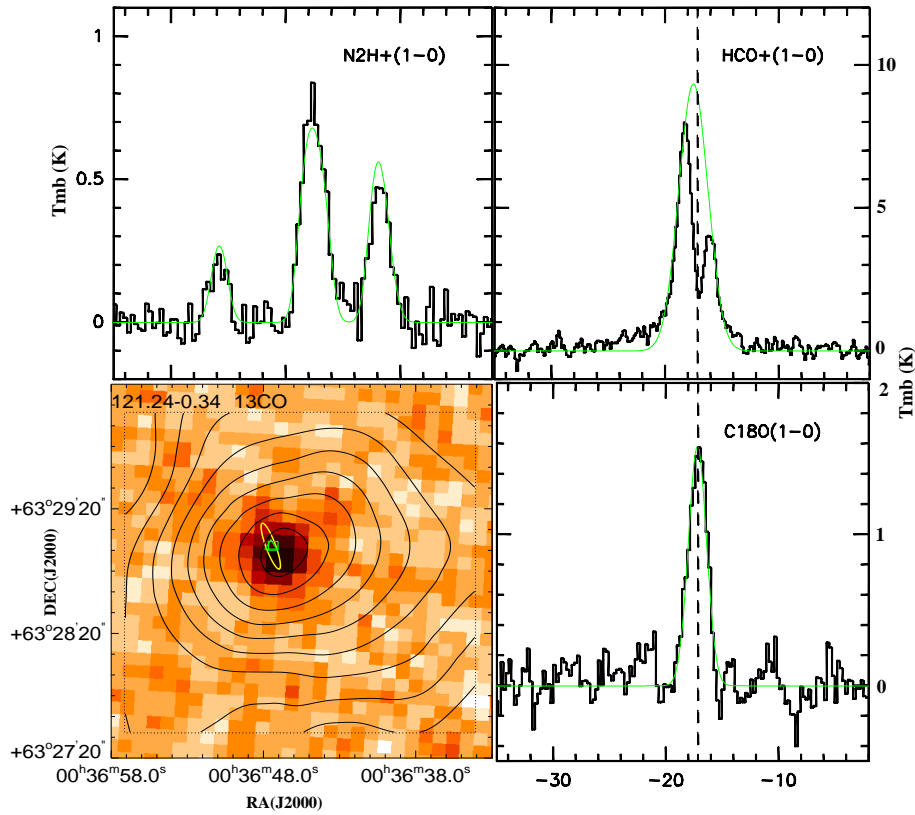


Fig. 3 N_2H^+ , HCO^+ and $C^{18}O$ characteristic spectra for 121.24–0.34 alongside the $^{13}CO(1-0)$ contours overlaid on the 21 μm MSX image. On the image, the square marks the 6.7-GHz CH_3OH maser, the triangle marks the H_2O maser and the ellipse denotes the error ellipse of the IRAS point source. Green lines are hyperfine structure/Gaussian fittings. The seven hyperfine components of N_2H^+ have blended into three groups due to large linewidths. The spectrum of HCO^+ reveals a self-absorbed line profile and is fitted with a Gaussian by masking the self-absorption dip.

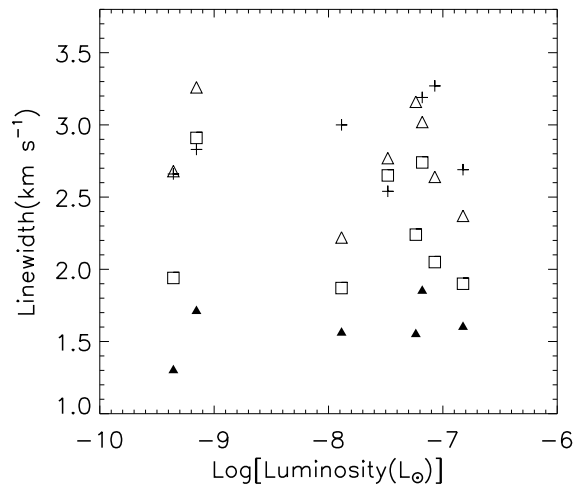


Fig. 4 Line width as a function of maser luminosity. Open triangles and squares indicate ^{13}CO and $C^{18}O$; pluses and filled triangles indicate HCO^+ and N_2H^+ .

Purcell et al. (2006, 2009)’s sample, which are composed of both high- and low-luminosity masers. Previous observations of ammonia also indicate that $\text{NH}_3(1,1)$ (2,2) linewidths of low-luminosity maser regions are smaller than those of high-luminosity maser regions (Paper I).

4.2 Gas Mass vs Virial Mass

In Figure 5 we plot the diagram of gas mass versus virial mass. For the maser associated cores, M_{gas} ranges from 25 to 250 M_{\odot} , with a mean value of 104 M_{\odot} and M_{vir} ranges from 13 to 220 M_{\odot} , with a mean value of 78 M_{\odot} . We can see that the value of M_{vir} and M_{gas} are consistent with having the same magnitude. As a general rule, clouds with $M_{\text{gas}}/M_{\text{vir}} > 1$ are considered to be gravitationally bound systems. Generally, we propose that cores that contain low-luminosity 6.7-GHz methanol masers should be gravitationally bound.

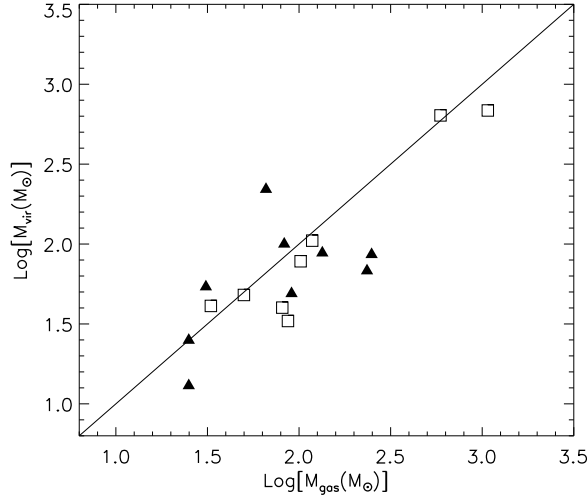


Fig. 5 Gas masses versus virial masses. Filled triangles and open squares denote cores with and without maser associations, respectively. The solid line is the line where M_{gas} equals M_{vir} .

4.3 Associations

Apart from Class II methanol masers, outflows, and bright IRAS sources, H_2O and OH masers are also signatures of star formation. Since our targeted sources are all methanol masers, it is meaningful to investigate the associations of methanol masers with other star-forming phenomena, such as outflows, bright IRAS sources and two other kinds of masers. In Table 8, we list these associations. The association rates for the IRAS source, outflow and H_2O are all 7/9, but the association rate for the OH maser is only 2/9. Positions of OH, H_2O and IRAS sources are also marked in Figure 2 to show their spatial coexistence. We can see that these low-luminosity methanol masers are highly coincident with bright IRAS sources, outflows and H_2O masers. In contrast, associations of OH masers are relatively weak. Though the number of studied cases in our sample is limited, our sample clearly indicates the fact that the Class II methanol maser phase is more likely to be overlaid on outflow and

Table 8 Associations of These Low-luminosity 6.7-GHz Masers

Source Name	IRAS Name	Outflow	H ₂ O	OH
106.80+5.31	22176+6303	Y [1]	Y [5]	Y [7]
111.25-0.77	23139+5939	Y [1]	Y [5]	N [8]
121.24-0.34	00338+6312	Y [1]	Y [5]	...
133.72+1.22	02219+6152	Y [1]	Y [5]	N [7]
183.35-0.59	05480+2545	N [2]	N [5]	...
188.80+1.03	06061+2151	N [3]	Y [5]	N [7]
189.03+0.78	06056+2131	Y [1]	Y [5]	N [7]
189.78+0.34	N	Y [4]	Y [6]	...
206.54-16.3	N	Y [1]	N [5]	Y [9]
Association Rate	7/9	7/9	7/9	2/9

Notes: “Y” indicates association, “N” indicates no association, “...” indicates that no information is available;

References — [1] Wu et al. (2004); [2] Snell et al. (1990); [3] Kim & Kurtz (2006); [4] Xu et al. (2006b); [5] Valdetaro et al. (2001); [6] Lada et al. (1981); [7] Baudry et al. (1997); [8] Szymczak & Kus (2000); [9] Knowles et al. (1976).

the H₂O maser phrase than to be overlaid on the OH maser phrase (Ellingsen et al. 2007; Breen et al. 2010).

5 CONCLUSIONS

We have performed multi-line observations, including transitions of ¹³CO(1–0), C¹⁸O(1–0), HCO⁺(1–0) and N₂H⁺(1–0), towards nine low-luminosity 6.7-GHz methanol masers. From integrated intensity emission maps, we identified 17 cores, among which nine cores are closely associated with low-luminosity masers and eight cores lack maser associations. Physical quantities of these cores were derived, including column densities, core sizes, masses and molecular abundances. Our major findings are as follows:

- (1) Linewidths of ¹³CO, HCO⁺ and N₂H⁺ of these low-luminosity maser regions are smaller than Purcell et al. (2006, 2009)’s sample.
- (2) A “blue profile” of the HCO⁺(1–0) spectrum, signature of inflow, is found towards one source, the detection rate of which is three times less than Wu et al. (2007).
- (3) N₂H⁺ abundances of these regions show larger fluctuations than those of CO.
- (4) Virial masses and gas masses of the maser associated cores are consistent with having the same magnitude, indicating that these cores that contains low-luminosity 6.7-GHz masers are gravitationally bound systems.
- (5) These low-luminosity masers are more inclined to coexist with H₂O masers, outflows and bright IRAS sources rather than to coexist with OH masers.

We however caution that the number of sources in our study is limited. Consequently, the findings of this work have to be confirmed by a much larger sample.

Acknowledgements We wish to thank all the staff at Qinghai Station of Purple Mountain Observatory for their assistance with our observations. This work was supported by the National Natural Science Foundation of China (Grant Nos. 10673024, 10733030, 10703010 and 10621303) and the National Basic Research Program of China-973 Program (2007CB815403).

References

- Baudry, A., Desmurs, J. F., Wilson, T. L., & Cohen, R. J. 1997, *A&A*, 325, 255
- Bergin, E. A., & Langer, W. D. 1997, *ApJ*, 486, 316
- Botschwina, P. 1984, *Chem. Phys. Lett.*, 107, 535
- Breen, S. L., Ellingsen, S. P., Caswell, J. L., & Lewis, B. E. 2010, *MNRAS*, 401, 2219
- Carpenter, J. M., Snell, R. L., & Schloerb, F. P. 1995, *ApJ*, 445, 246
- Caswell, J. L., Vaile, R. A., Ellingsen, S. P., Whiteoak, J. B., & Norris, R. P. 1995, *MNRAS*, 272, 96
- Caswell, J. L. 2009, *PASA*, 26, 454
- Chandler, C. J., & Carlstrom, J. E. 1996, *ApJ*, 466, 338
- Crampton, D., & Fisher, W. A. 1974, *PDAO*, 14, 283
- Ellingsen, S. P., Voronkov, M. A., Cragg, D. M., Sobolev, A. M., Breen, S. L., & Godfrey, P. D. 2007, *IAUS*, 242, 213
- Ellingsen, S. P. 2007, *MNRAS*, 377, 571
- Emprechtinger, M., Wiedner, M. C., Simon, R., et al. 2009, *A&A*, 496, 731
- Fuller, G. A., Williams, S. J., & Sridharan, T. K. 2005, *A&A*, 442, 949
- Georgelin, Y. M., & Georgelin, Y. P. 1976, *A&A*, 49, 57
- Green, J. A., Caswell, J. L., Fuller, G. A., et al. 2009, *MNRAS*, 392, 783
- Hildebrand, R. H. 1983, *QJRAS*, 24, 267
- Hughes, V. A., & MacLeod, G. C. 1993 *AJ*, 105, 1495
- Humphreys, R. M. 1978, *ApJS*, 38, 309
- Kim, K. T., & Kurtz, S. E. 2006, *ApJ*, 643, 978
- Klaassen, P. D., & Wilson, C. D. 2007, *ApJ*, 663, 1092
- Knowles, S. H., Caswell, J. L., & Goss, W. M. 1976, *MNRAS*, 175, 537
- Lada, C. J., Blitz, L., Reid, M. J., & Moran, J. M. 1981, *ApJ*, 243, 769
- Langer, W. D., van Dishoeck, E. F., Bergin, E. A., Blake, G. A., Tielens, A. G. G. M., Velusamy, T., & Whittet, D. C. B. 2000, in *Protostars and Planets IV* (Tucson: Univ. Arizona Press), 29
- Larionov, G. M., Val'tts, I. E., Winnberg, A., Johansson, L. E. B., Booth, R. S., & Golubev, V. V. 1999, *A&AS*, 139, 257
- Lovas, F. J., & Krupenie, P. H. 1974, *J. Phys. Chem. Ref. Data*, 3, 245
- MacLeod, G. C., van der Walt, D. J., North, A., Gaylard, M. J., Galt, J. A., & Moriarty-Schieven, G. H. 1998 *AJ*, 116, 2936
- MacLaren, I., Richardson, K. M., & Wolfendale, A. W. 1988, *ApJ*, 333, 821
- Mezger, P. G., Chini, R., Kreysa, E., Wink, J. E., & Salter, C. J. 1988, *A&A*, 191, 44
- Mezger, P. G., Sievers, A. W., Haslam, C. G. T., Kreysa, E., Lemke, R., Mauersberger, R., & Wilson, T. L. 1992, *A&A*, 256, 631
- Motogi, K., Watanabe, Y., Sorai, K., et al. 2008, *MNRAS*, 390, 532
- Minier, V., Ellingsen, S. P., Norris, R. P., & Booth, R. S. 2003, *A&A*, 403, 1095
- Pandian, J. D., Goldsmith, P. F., & Deshpande, A. A. 2007, *ApJ*, 656, 255
- Pavlakis, K. G., & Kylafis, N. D. 1996a, *ApJ*, 467, 300
- Pavlakis, K. G., & Kylafis, N. D. 1996b, *ApJ*, 467, 309
- Pestalozzi, M. R., Minier, V., & Booth, R. S. 2005, *A&A*, 432, 737
- Pineda, J. E., Caselli, P., & Goodman, A. A. 2008 *ApJ*, 679, 481
- Purcell, C. R., Balasubramanyam, R., Burton, M. G., et al. 2006, *MNRAS*, 367, 553
- Purcell, C. R., Longmore, S. N., Burton, M. G., Walsh, A. J., Minier, V., Cunningham, M. R., & Balasubramanyam, R. 2009, *MNRAS*, 394, 323
- Reid, M. J., Menten, K. M., Zheng, X. W., et al. 2009, *ApJ*, 700, 137
- Scoville, N. Z., Sargent, A. I., Sanders, D. B., Claussen, M. J., Masson, C. R., Lo, K. Y., & Phillips, T. G. 1986, *ApJ*, 303, 416

- Slysh, V. I., Val'ts, I. E., Kalenskii, S. V., Voronkov, M. A., Palagi, F., Tofani, G., & Catarzi, M. 1999, *A&AS*, 134, 115
- Snell, R. L., Dickman, R. L., & Huang, Y. L. 1990, *ApJ*, 352, 139
- Szymczak, M., Hrynek, G., & Kus, A. J. 2000, *A&AS*, 143, 269
- Szymczak, M., & Kus, A. J. 2000, *A&AS*, 147, 181
- Sun, Y. & Gao, Y. 2009, *MNRAS*, 392, 170
- Torrelles, J.M., Patel, N., Gómez, J. F., Anglada, G., & Uscanga, L. 2005, *Ap&SS* 295, 53
- Valdettaro, R., Palla, F., Brand, J., et al. 2001, *A&A*, 368, 845
- Williams, J. P., de Geus, E. J. & Blitz, L. 1994, *ApJ*, 428, 693
- Womack, M., Ziurys, L. M., & Wyckoff, S. 1992, *ApJ*, 387, 417
- Wu, Y., Wei, Y., Zhao, M., Shi, Y., Yu, W., Qin, S., & Huang, M. 2004, *A&A*, 426, 503
- Wu, Y. F., Henkel, C., Xue, R., Guan, X., & Miller, M. 2007, *ApJ*, 669, L37
- Wu, Y. W., Xu, Y., Yang, J., & Li, J. J. 2009, *RAA (Research in Astronomy and Astrophysics)*, 9, 1343
- Wu, Y. W., Xu, Y., Pandian, J. D., Yang, J., Henkel, C., Menten, K. M., & Zhang, S. B. 2010, *ApJ*, 720, 392
(Paper I)
- Xu, Y., Zheng, X. W., & Jiang, D. R. 2003, *ChJAA (Chin. J. Astron. Astrophys.)*, 3, 49
- Xu, Y., Reid, M. J., Zheng, X. W., & Menten, K. M. 2006a, *Science*, 311, 54
- Xu, Y., Shen, Z. Q., Yang, J., et al. 2006b, *AJ*, 132, 20
- Xu, Y., Li, J. J., Hachisuka, K., Pandian, J. D., Menten, K. M., & Henkel, C. 2008, *A&A*, 485, 729
- Xu, Y., Voronkov, M. A., Pandian, J. D., Li, J. J., Sobolev, A. M., Brunthaler, A., Ritter, B., & Menten, K. M. 2009, *A&A*, 507, 1117
- Yang, J., Umemoto, T., Iwata, T., & Fukui, Y. 1991, *ApJ*, 373, 137
- Zuo, Y. X., Yang, J., Shi, S. C., Chen, S. H., Pei, L. B., Yao, Q. J., Sun, J. J., & Lin, Z. H. 2004, *ChJAA (Chin. J. Astron. Astrophys.)*, 4, 390